



# Corrosion protection of steel cut-edges by hot-dip galvanized Al(Zn,Mg) coatings in 1 wt% NaCl: Part II. Numerical simulations

Olga Dolgikh<sup>1</sup> | Hans Simillion<sup>1</sup> | Sviatlana V. Lamaka<sup>2,3</sup> |  
Alexandre C. Bastos<sup>4</sup> | Huibin B. Xue<sup>2</sup> | Maryna G. Taryba<sup>2</sup> |  
Andre R. Oliveira<sup>4</sup> | Christian Allély<sup>5</sup> | Bart Van Den Bossche<sup>6</sup> |  
Krista Van Den Bergh<sup>7</sup> | Joost De Strycker<sup>7</sup> | Johan Deconinck<sup>1</sup>

<sup>1</sup> Research group SURF, Vrije Universiteit Brussel, Pleinlaan 2, 1050 Brussels, Belgium

<sup>2</sup> Centro de Química Estrutural, Instituto Superior Técnico, Universidade de Lisboa, Av. Rovisco Pais, 1049-001 Lisbon, Portugal

<sup>3</sup> MagIC, Institute of Materials Research, Magnesium Innovation Centre, Helmholtz-Zentrum Geesthacht, 21502, Germany

<sup>4</sup> DEMaC/CICECO, Universidade de Aveiro, Campus Universitário de Santiago, 3810-193 Aveiro, Portugal

<sup>5</sup> ArcelorMittalMaizièresResearch, Voie Romaine, 57283 Maizières-les-Metz, France

<sup>6</sup> Elsyca N.V., Vaartdijk 3/603, B-3018 Wijgmaal, Belgium

<sup>7</sup> OCAS N.V., J.F. Kennedylaan 3, B-9060 Zelzate, Belgium

## Correspondence

Hans Simillion, Research group SURF, Vrije Universiteit Brussel, Pleinlaan 2, 1050 Brussels, Belgium.  
Email: hsimilli@vub.ac.be; hanssimi@gmail.com

In this paper a mechanistic model is elaborated to simulate the corrosion behavior of aluminum–zinc–magnesium coatings on steel. The model is based on the mass transport and reactions of the ions in the electrolyte (MITReM). The finite element method has been used, which allows to perform time-dependent simulations with micrometer scale to study local corrosion effects. The formation of corrosion products and the prediction of electrolyte concentration distributions are compared for different metallic coating compositions. The spatial and temporal simulation of complex precipitates provides an additional tool to validate the model through corrosion product characterization. The simulation results are compared to experimental observations, presented in part I of this paper. The MITReM simulations are limited to the micro-scale and therefore to small geometries. A link is made with the potential model which can be applied on macro-scale objects. A qualitative agreement is found between the simulations at both scales and the experiments. Further quantification of this model would optimize the simulations for material design and for predictive maintenance.

## KEYWORDS

Al(Zn Mg) alloys, cut-edge corrosion, multi-ion modeling

## 1 | INTRODUCTION

Corrosion of cut-edges of steel sheets with a metallic coating is a form of galvanic corrosion where the coating often serves as a sacrificial anode with respect to the metal it is applied on. This can provide a galvanic protection, which is driven by the potential difference between the metal and the coating, where the reactivity of the coating plays an important role. For that reason, Zn and its alloys are used as protective coatings for

steel more often than pure aluminum coatings. The context of this research is the development of mechanistic corrosion models toward the development of metallic coatings that combine barrier properties with cathodic protection.

Great progress has been made in the field of mechanistic corrosion modeling over the last decades. Early simulations rely on the potential model and are limited in their application due to the requirement of homogeneous electrolyte conditions. Palani et al.<sup>[1]</sup> have

applied the potential model for the galvanic corrosion between carbon fiber reinforced polymers and aluminum alloys for aerospace applications. The potential model is limited to simulations of potential distributions only, but it can nevertheless predict main areas of corrosion in the design phase. Thébault et al.<sup>[2,3]</sup> combined the potential model with oxygen diffusion calculations and found good correlations by comparing the simulation results with SVET experiments. Another improvement of the potential model is the extension with a porous electrode model studied by Venkatraman et al.<sup>[4]</sup> With a similar approach Hoerlé et al.<sup>[5]</sup> considered a porous rust layer and its transformations that influences the corrosion process of steel.

A limitation of the potential model and its derivative models is that they do not consider the (local) composition of the electrolyte. The more comprehensive multi-ion transport and reaction model (MITReM) combines the potential distribution calculations with the mass balance equations for all (relevant) species/ions in the electrolyte. This allows for the local and time dependent prediction of the formed corrosion products and, for example, pH distribution. Such models have been applied by Thébault et al.<sup>[6]</sup> for the study of corrosion of galvanized steel under thin film electrolytes. Topa et al.<sup>[7]</sup> performed a similar study, but for thicker electrolyte layers. They introduced an artificial flow to mimic the natural convection in the electrolyte, which avoids flow calculations and simplifies the calculations. Dolgikh et al.<sup>[8]</sup> have applied the concept of the micro-turbulent diffusion term to take the natural convection and diffusion layer into account. Their approach consists in making a modification to each diffusion coefficient. This concept is further elaborated in the model description.

In the first part of the present work, corrosion performance of the cut-edges of steel protected by Al-based alloy coatings in 1 wt% NaCl is studied with a number of electrochemical and surface analysis techniques. It has been found that metallic coatings, with different zinc content; AlZn0, AlZn10, and AlZn30Mg4; show non-uniform (in time) corrosion activity due to their complex multi-phase microstructure. During galvanostatic dissolution, AlZn30Mg4 showed a selective dissolution of a Zn<sub>2</sub>Mg phase while the other two alloy coatings dissolve uniformly. During immersion, few very active corrosion sites could be detected along the surface of a coating at any moment, while the rest surface remained inactive. The activity of these “active spots” changed stochastically in time leading to the subsequent change in local electrolyte composition. Composition and localization of solid corrosion products on the cut-edge surface is established by a set of experimental techniques. These corrosion products do not slow down either cathodic or anodic reactions on a cut-edge unlike discussed earlier for zinc-based coatings.

The experimental data served as quantitative and qualitative input for two numerical models with different level of detail that describe corrosion process in the studied systems on micro- and macro scale. In this contribution, the models are described and their results are presented, discussed, and compared with the experimental observations.

A combination of the experimental work with the multi-scale models is applied on the steel cut-edges. Newly developed hot-dip galvanized aluminum-based coatings are studied during immersion in a 1 wt% NaCl electrolyte. Part I of this work<sup>[9]</sup> described experimental results used for setting up the model. Present work (Part II) shows the modeling approach and validation.

A mechanistic model that includes ionic concentrations has the benefit that these concentrations can be used to predict chemical reactions and corrosion products. But this complexity comes at a cost of longer computational times. To overcome this limitation the potential model is applied on a macro-scale cut-edge to simulate the run-off of the metallic coating.

## 2 | DESCRIPTION OF THE SYSTEM

Corrosion of steel cut-edges protected by aluminum-based coatings in chloride media is a complex process, which is determined not only by electrochemical reactions taking place on the metal surface, but also by the local pH changes and formation of soluble and insoluble corrosion products. The proposed model (MITReM) is an application of the transport model extended with the reaction terms. The calculation of the local concentrations and potential are validated with the local in-situ electrochemical measurements.

The coatings are applied on a cold rolled steel substrate in a laboratory environment. The applied metallic coatings have a typical thickness around 15 μm. SEM images have been taken in combination with EDX-mappings to determine the composition of the coating (see Figure 1). SEM images of the cross section provide a view on the coating structure, phase distribution, and thickness of different phases.

The coating compositions are based on a typical industrial aluminum coating. The resulting coatings studied in this work are identified in Table 1.

## 3 | SIMULATIONS ON THE MICRO-SCALE: MULTI-ION TRANSPORT AND REACTION MODEL

On the micro-scale (laboratory) level it is possible to take into account these phenomena by building so called MITReM.

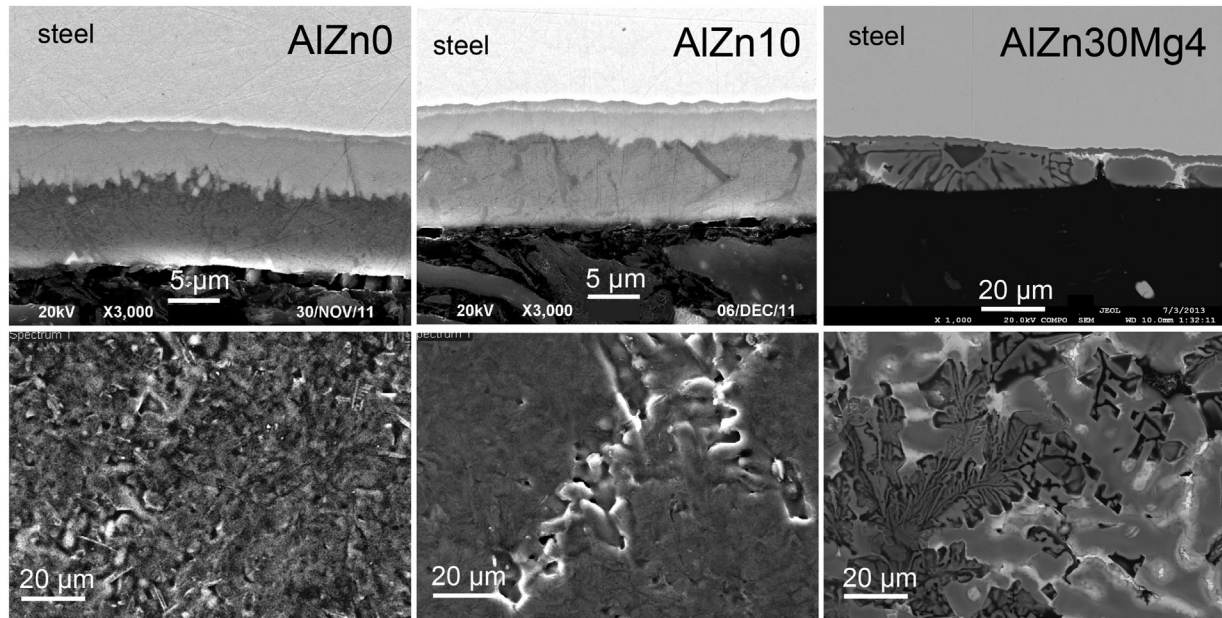


**FIGURE 1** Microstructure of the studied aluminum-based coatings: SEM micrographs of the cut-edge cross-sections (top row) and top views of the coatings (bottom row). Reproduced from ref. [9]

The governing equations and the system setup are discussed next.

### 3.1 | Governing equations

The governing equations of the MITReM are a set of balance equations for each species (Eq. (1)) and the electroneutrality condition (Eq. (2)).

$$\sum_{r=1}^R v_r s_{kr} = D_k \nabla^2 c_k + \frac{z_k F D_k c_k}{RT} \nabla^2 U + D_{\mu\text{conv}}^{\text{ref}} \nabla^2 c_k \quad (1)$$

$$\sum_{k=1}^K z_k c_k = 0 \quad (2)$$

where  $c_k$ ,  $z_k$ ,  $D_k$  are respectively the concentration ( $\text{mol m}^{-3}$ ), charge ( $-$ ) and diffusion coefficient ( $\text{m}^2 \text{s}^{-1}$ ) of species  $k$ .  $s_{kr}$  is the stoichiometric coefficient of species  $k$  in reaction  $r$  and  $v_r$  is the reaction rate of reaction  $r$ .  $F$  is the Faraday constant

( $\text{C mol}^{-1}$ ),  $R$  the universal gas constant ( $\text{J mol}^{-1} \text{K}^{-1}$ ),  $T$  the temperature ( $\text{K}$ ) and  $U$  is the electrolyte potential ( $\text{V}$ ).

The simulations are performed at steady-state ( $\frac{\partial c_k}{\partial t} = 0$ ). The reaction term ( $\sum_{r=1}^R v_r s_{kr}$ ) is taken into account for the prediction of the corrosion products.

The left-side term of the Eq. (1) is the production/consumption of species  $k$  in chemical reactions. The first and the second terms on the right side describe the transport of species in the electrolyte by means of diffusion and migration, respectively. The last term is a so called micro-convection term, which describes a small motion of species due to the temperature gradient, vibrations, etc. The concept of micro-convection is first introduced by Amatore et al. [10] and later further developed by some of the authors in a recent publication. [8] In that work a correction is proposed for when multiple species are considered and the micro-convection term has to become species independent. The micro-convection coefficient,  $D_{\mu\text{conv}}^{\text{ref}}$  ( $\text{m}^2 \text{s}^{-1}$ ) is expressed as:

$$D_{\mu\text{conv}}^{\text{ref}} = 1.5072 \cdot D^{\text{ref}} \left( \frac{d}{\delta^{\text{ref}}} \right)^4 \quad (3)$$

where  $D^{\text{ref}}$  and  $\delta^{\text{ref}}$  are, respectively the diffusion coefficient ( $\text{m}^2 \text{s}^{-1}$ ) and the diffusion layer thickness ( $m$ ) of a reference species.

$D_{\mu\text{conv}}$  is independent of the nature of species  $k$ , and dependent only on  $d$ , the distance to the electrode and properties of a reference species. In this model, oxygen is chosen as reference species, since  $\delta_{\text{O}_2}^{\text{ref}}$  can be easily derived from the experimental polarization curves. Here  $D_{\mu\text{conv}}^{\text{ref}} = 2 \times 10^{-9} \text{m}^2 \text{s}^{-1}$  and  $\delta^{\text{ref}} = 250 \mu\text{m}$ .

**TABLE 1** Coatings studied in this work

Name	Description
AlZn0	Aluminum coating, considered as the reference aluminum coating (reference)
AlZn10	Reference coating composition, with 10 wt% zinc in the bath
AlZn30Mg4	Reference coating composition, with 30 wt% zinc and 4 wt% magnesium

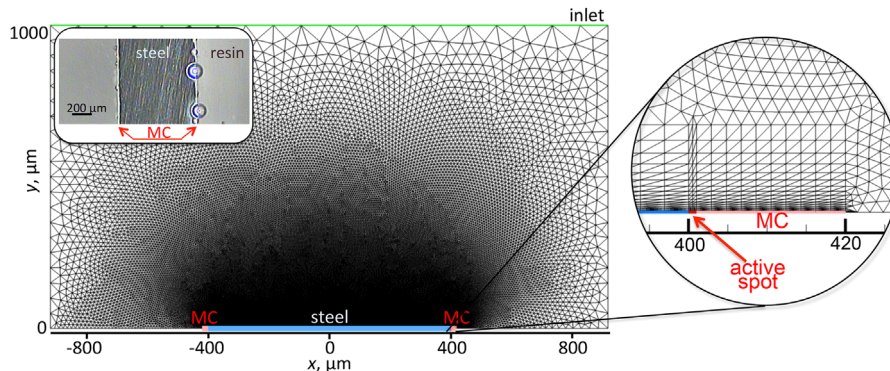


**FIGURE 2** Computation domain used for MITReM simulations. Inset: top-view optical micrograph of the cut-edge geometry. [Color figure can be viewed at [wileyonlinelibrary.com](http://wileyonlinelibrary.com)]

### 3.2 | Geometry and boundary conditions

Due to the high aspect ratio, the real cut-edge geometry can be approximated by the two-dimensional computational domain shown in Figure 2. The electrodes – 800  $\mu\text{m}$  steel (cathode) in between two 20  $\mu\text{m}$  metallic coatings, MC (anodes) – are placed on the bottom of the geometry. The height of the domain represents the electrolyte layer thickness. Due to the presence of micro-convection, electrolyte is well-mixed already at a distance  $> 3 \delta^{\text{ref}}$  and can be considered as a bulk solution.<sup>[8]</sup> Hence, 1 mm high domain is a good approximation for immersed conditions. The top boundary is an inlet. Other boundaries are insulators. For FEM calculation, the computational domain is discretized in 38 003 nodes (75 566 triangle elements) with the refining around working electrode. Simulations are performed using the in-house developed software *MuPhyS*.

At the electrolyte-air interface (inlet) bulk concentrations of all species except for oxygen and carbon dioxide are imposed:

$$c_k = c_k^{\text{bulk}} \quad (4)$$

The dissolution rates of O<sub>2</sub> and CO<sub>2</sub> are given by expression:

$$\frac{\partial c_k}{\partial n} = F_k^{\text{max}} \left( 1 - \frac{c_k}{c_k^{\text{sat}}} \right) \quad (5)$$

with  $F_k^{\text{max}}$  the maximum dissolution rate of O<sub>2</sub> or CO<sub>2</sub>,  $c_k$  the local gas concentration and  $c_k^{\text{sat}}$  is the gas solubility in an aqueous NaCl solution. At 25 °C,  $F_{\text{O}_2}^{\text{max}} = 3.5 \times 10^{-5} \text{ mol m}^{-2} \text{ s}^{-1}$ <sup>[6]</sup> and  $F_{\text{CO}_2}^{\text{max}} = 4 \times 10^{-7} \text{ mol m}^{-2} \text{ s}^{-1}$ <sup>[11]</sup>.

At the electrodes, the fluxes of non-electroactive species normal to the electrode surface are zero. For electroactive species, the fluxes ( $\vec{N}_k \cdot \vec{1}_n$ ) are given by the rates of the electrochemical reactions:

$$\vec{N}_k \cdot \vec{1}_n = - \sum_{e=1}^E v_e s_{ke} \quad (6)$$

with  $v_e$  the rate of the electrode reaction,  $s_{ke}$  the stoichiometric coefficient of species  $k$  in reaction  $e$ .

In this work, electrode reactions are considered as irreversible and their rates are given by the Tafel Eq. (7) or by linearized polarization curves (8):

$$v_e = -k_{\text{red}} = \exp \left[ - \frac{nF\alpha_{\text{red}}}{RT} (V - U) \right] c_{\text{ox}} \quad (7)$$

$$v_e = \frac{A(V - U) + B}{nF} \quad (8)$$

with  $k_{\text{red}}$  the reaction rate constant,  $n$  the number of electrons transferred,  $\alpha_{\text{red}}$  the charge transfer coefficient and  $V$  the electrode potential ( $V$ ).  $A$  and  $B$  are fitted parameters.

The total current density is the sum of partial currents of the electrochemical reactions taking place at the working electrode.

$$J_{\text{tot}} = \sum_{e=1}^E J_e = F \sum_{e=1}^E n_e v_e \quad (9)$$

At the insulating walls, normal flux of species and potential gradients are set to zero:

$$\vec{N}_k \cdot \vec{1}_n = 0, \partial U / \partial n = 0 \quad (10)$$

### 3.3 | Input parameters

The input parameters for MITReM are defined based on the experimental results described in the Part I of this work.<sup>[9]</sup> Remark, however, that when solving the equations using FEM, the number of unknowns in the system is defined by the total number of species  $K$  and the number of the mesh nodes. Therefore, in order to build a manageable multi-ion model,

**TABLE 2** Species considered in the MITReM with their charges, diffusivities and bulk concentrations

Species	$z_k$	$D_k \times 10^9 \text{ m}^2 \text{ s}^{-1}$	$c_k^{\text{bulk}}$	Species	$z_k$	$D_k \times 10^9 \text{ m}^2 \text{ s}^{-1}$	$c_k^{\text{bulk}}$
Na <sup>+</sup>	+1	1.23 <sup>[13]</sup>	$1.71 \times 10^2$	Fe <sup>2+</sup>	+2	0.65	$1.00 \times 10^{-6}$
Cl <sup>-</sup>	-1	1.19 <sup>[13]</sup>	$1.71 \times 10^2$	Fe(OH) <sup>+</sup>	-1	0.50	$1.00 \times 10^{-10}$
H <sup>+</sup>	+1	9.31 <sup>[13]</sup>	$3.16 \times 10^{-3}$	Fe(OH) <sub>2</sub>	0	0.50	$1.00 \times 10^{-11}$
OH <sup>-</sup>	-1	5.26 <sup>[13]</sup>	$3.16 \times 10^{-6}$	Zn <sup>2+</sup>	+2	0.70 <sup>[14]</sup>	$1.00 \times 10^{-7}$
O <sub>2</sub>	0	1.96 <sup>[14]</sup>	$2.43 \times 10^{-1}$	Zn(OH) <sup>+</sup>	+1	0.65	$1.00 \times 10^{-8}$
Al <sup>3+</sup>	+3	0.541 <sup>[15]</sup>	$1.00 \times 10^{-6}$	Zn(OH) <sub>2</sub>	0	0.65	$1.00 \times 10^{-9}$
Al(OH) <sup>2+</sup>	+2	0.541	$6.10 \times 10^{-6}$	CO <sub>2</sub>	0	1.91 <sup>[14]</sup>	$3.68 \times 10^1$
Al(OH) <sub>2</sub> <sup>+</sup>	+1	0.541	$1.10 \times 10^{-5}$	H <sub>2</sub> CO <sub>3</sub>	0	1.50	$1.21 \times 10^{-3}$
Al(OH) <sub>3</sub>	0	0.541	$3.30 \times 10^{-7}$	HCO <sub>3</sub> <sup>-</sup>	-1	1.19 <sup>[14]</sup>	$1.08 \times 10^{-6}$
Al(OH) <sub>4</sub> <sup>-</sup>	-1	0.541	$4.70 \times 10^{-8}$	CO <sub>3</sub> <sup>2-</sup>	-2	0.92 <sup>[14]</sup>	$1.00 \times 10^{-11}$

discrimination between all possible species, chemical and electrode reactions has to be done. Furthermore, on the chosen level of details it is impossible to take into account all the phenomena found when setting up the model and certain simplifications are required.

The set of relevant species is chosen based on the analysis of thermodynamic diagrams built using the HYDRA-MEDUSA software<sup>[12]</sup> and the precipitated corrosion products identified experimentally in part I.<sup>[9]</sup>

- The set of chemical and electrochemical reactions considered in the model is the minimum set required to adequately reproduce experimental observations.
- The details of the coatings microstructure (see Figure 2, part I) are not considered in the model. The coating is seen as an entity with averaged electrochemical properties. This is justified as the potential difference between steel and the coating is much higher than the potential difference between phases
- The presence of active corrosion zones is mimicked by introducing a segment (“active spot”) within the metallic coating where the average rate constants of the electrode reactions are arbitrarily increased with the factor 50. If no “active spot” is considered in the simulations, only half of the geometry depicted in Figure 2 is considered due its symmetry.
- For simplification, the stochastic nature of the corrosion process is neglected. The simulation are performed for the stationary situation where no active corrosion spots die and no new active spots appear in time.
- No surface coverage by corrosion products is envisioned in the model as no experimental evidence of their blocking action has been found experimentally, see part I.

### 3.3.1 | Relevant species

Soluble species considered in the model are listed in Table 2 together with their diffusivity coefficient, charge numbers

and initial (bulk) concentrations. Diffusion coefficients are taken from literature (if available) and adjusted to match the measured electrolyte conductivity. Solid corrosion products include insoluble metal hydroxides Fe(OH)<sub>2(s)</sub>, Zn(OH)<sub>2(s)</sub>, Al(OH)<sub>3(s)</sub>, iron oxyhydroxide FeOOH<sub>(s)</sub>, simonkolleite Zn<sub>5</sub>(OH)<sub>8</sub>Cl<sub>2(s)</sub>, hydrozincite Zn<sub>5</sub>(OH)<sub>6</sub>(CO<sub>3</sub>)<sub>2(s)</sub>, aluminum hydroxichloride Al(OH)<sub>2</sub>Cl<sub>(s)</sub>, and layered double hydroxide Mg<sub>6</sub>Al<sub>2</sub>(OH)<sub>12</sub>CO<sub>3(s)</sub>. Their diffusion coefficients are assumed to be equal to  $1 \times 10^{-11} \text{ m}^2 \text{ s}^{-1}$  and initial concentrations are  $1 \times 10^{-12} \text{ mol m}^{-3}$ .

### 3.3.2 | Electrode and chemical reactions

The electrochemical reactions that are taken into account in the model include dissolution of the coating (Eq. (11)) and steel (Eq. (12)) as anodic reactions and reduction of the dissolved oxygen (Eq. (13)) and hydrogen evolution on steel (Eq. (14)) as cathodic ones:

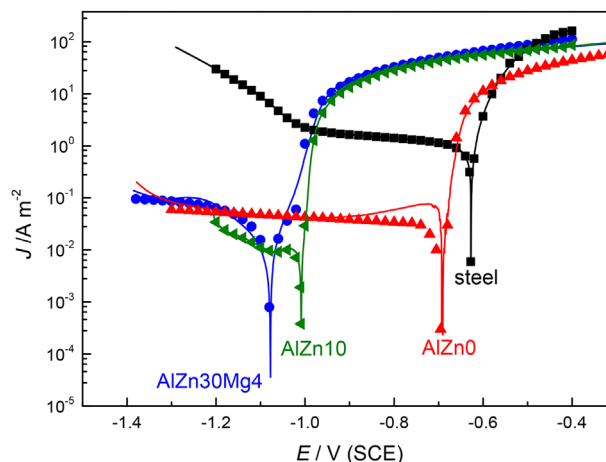
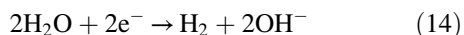
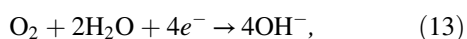
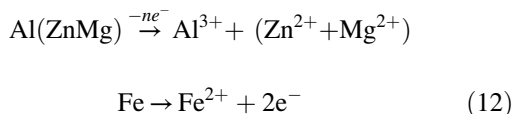


**FIGURE 3** Measured (lines) and simulated (symbols) global polarization curves obtained on steel, AlZn0, AlZn10, and AlZn30Mg4 samples in 1 wt% NaCl (pH 7). [Color figure can be viewed at [wileyonlinelibrary.com](http://wileyonlinelibrary.com)]

**TABLE 3** Kinetic parameters of the electrode reactions considered in the MITReM

Reaction	Tafel polarization		Linear polarization	
	$k_{\text{red(ox)}}$	$\alpha_{\text{red(ox)}}$	A	B
O <sub>2</sub> reduction on steel	$2.5 \times 10^{-6}$	0.150	–	–
H <sub>2</sub> evolution on steel	$3.0 \times 10^{-11}$	0.175	–	–
Mg dissolution	$2.0 \times 10^{-3}$	0.096	–	–
AlZn30 matrix dissolution	–	–	159.95	147.06
AlZn10 matrix dissolution	–	–	137.90	137.90
AlZn0 matrix dissolution	–	–	163.55	109.26
Iron dissolution	–	–	919.58	536.77



The kinetic parameters of the electrode reactions are first roughly estimated by the manual fitting of the polarization curves recorded on steel and Al-based alloy coatings in 1 wt% NaCl and further adjusted by simulating the polarization curves with full set of species to match the measurements (Details on the polarization measurement are provided in part I of this work).<sup>[9]</sup> The quality of the fit is shown in Figure 3 and the kinetic parameters used for simulations are listed in Table 3.

The partial dissolution rates are measured with AESEC. The obtained flow rates of the dissolved ions are shown in Figure 4, which also confirms the selective nature of the dissolution of the AlZn30Mg4 alloy. When constant current of 60 A m<sup>-2</sup> is applied, only magnesium and zinc ions are detected in the solution in the first 1000 s suggesting the

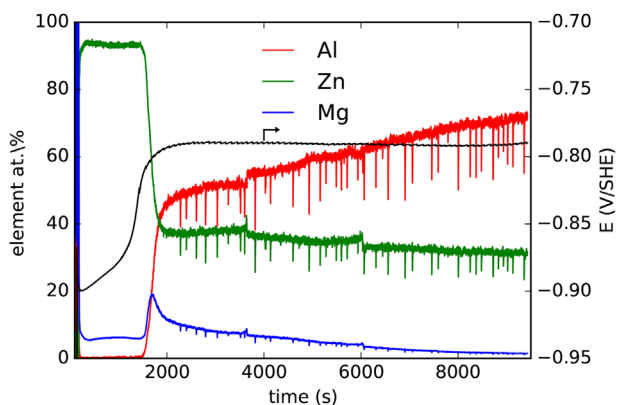


**FIGURE 4** Fraction of the elements dissolved from AlZn30Mg4 coating during galvanostatic anodic polarization ( $J = 60 \text{ A m}^{-2}$ ) in 1 wt% NaCl. Reproduced from ref. <sup>[9]</sup>. [Color figure can be viewed at wileyonlinelibrary.com]

preferential dissolution of a magnesium-rich phase. Afterwards, the amount of Mg<sup>2+</sup> in the electrolyte decreases, and Zn<sup>2+</sup> ions together with the increasing amount of Al<sup>3+</sup> ions are found indicating the dissolution of the Al-Zn matrix (Figure 4). The AlZn0 and AlZn10 (not shown) coatings dissolve uniformly according to the coating composition.

Based on the observed selective dissolution, partial oxidation reaction rates can be quantified. The partial polarization contributions are taken into account by decomposing the global polarization curve:

$$J_{\text{AlZn30Mg4}} = J_{\text{Mg}} + J_{\text{AlZn30}} \quad (15)$$

and

$$J_{\text{Zn}} = 0.3 \times J_{\text{AlZn30}}; \quad J_{\text{Al}} = 0.7 \times J_{\text{AlZn30}} \quad (16)$$

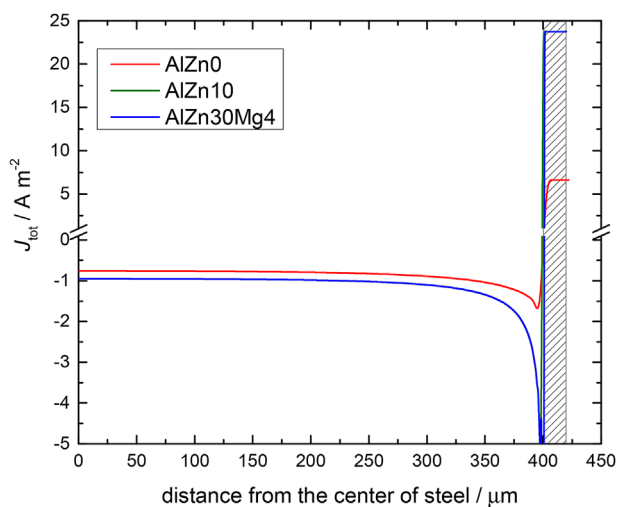
Chemical reactions chosen for the model include the water dissociation reaction, dissolution of CO<sub>2</sub> and its hydrolysis, stepwise hydrolysis of the metal ions and formation of solid corrosion products (Table 4). The rate constants,  $k_f$  and  $k_b$ , of chemical reactions are taken from literature when possible<sup>[16,15]</sup> or derived from the corresponding equilibrium constants,  $K_{\text{eq}}$ <sup>[12,17,18]</sup> such that the ratio  $k_f/k_b = K_{\text{eq}}$  is satisfied.

### 3.4 | MITReM simulation results and its comparison with the experiments

First simulations are performed for the situation when the activity of metallic coatings on both sides of steel is symmetrical. Simulated current distributions along the cut-edge surface for three studied coatings are shown in Figure 5. Interesting to note that AlZn0 coating is much less active in comparison to others leading to a lower oxygen reduction current. Cut-edge corrosion potentials,  $E_{\text{ce}}$ , shift to the negative direction in order AlZn0–AlZn10–AlZn30Mg4 (see Table 5). Remark, that obtained values of  $E_{\text{ce}}$  are in good qualitative agreement with measurements. However quantitatively, the simulated values of the cut-edge potentials are

**TABLE 4** Chemical reactions considered in the model and their rate constants

Reaction	$k_f$	$k_b$
$\text{H}_2\text{O} \rightleftharpoons \text{H}^+ + \text{OH}^-$	$1.5^{\text{a}, [15,16]}$	$2.5 \times 10^{8\text{b}, [15,16]}$
$2\text{H}^+ + \text{CO}_3^{2-} \rightleftharpoons \text{CO}_2 + \text{H}_2\text{O}$	$1.41 \times 10^{5\text{c}}$	$1.0 \times 10^{-4\text{b}}$
$\text{H}^+ + \text{CO}_3^{2-} \rightleftharpoons \text{HCO}_3^-$	$2.13 \times 10^{4\text{b}}$	$1.0 \times 10^{-3\text{a}}$
$\text{H}^+ + \text{HCO}_3^- \rightleftharpoons \text{H}_2\text{CO}_3$	$2.25 \times 10^{4\text{b}}$	$1.0 \times 10^{1\text{a}}$
$\text{Al}^{3+} + \text{H}_2\text{O} \rightleftharpoons \text{Al}(\text{OH})^{2+} + \text{H}^+$	$1.09 \times 10^{5\text{b}, [15]}$	$4.4 \times 10^{6\text{b}, [15]}$
$\text{Al}(\text{OH})^{2+} + \text{H}_2\text{O} \rightleftharpoons \text{Al}(\text{OH})_2^+ + \text{H}^+$	$1.09 \times 10^{5\text{b}, [15]}$	$4.4 \times 10^{6\text{b}, [15]}$
$\text{Al}(\text{OH})_2^+ + \text{H}_2\text{O} \rightleftharpoons \text{Al}(\text{OH})_{3(\text{aq})} + \text{H}^+$	$1.58 \times 10^{3\text{b}}$	$1.0 \times 10^{7\text{b}}$
$\text{Al}(\text{OH})_{3(\text{aq})} + \text{H}_2\text{O} \rightleftharpoons \text{Al}(\text{OH})_4^- + \text{H}^+$	$1.58 \times 10^{2\text{b}}$	$1.0 \times 10^{6\text{b}}$
$\text{Fe}^{2+} + \text{H}_2\text{O} \rightleftharpoons \text{Fe}(\text{OH})^+ + \text{H}^+$	$6.31 \times 10^{3\text{b}}$	$1.0 \times 10^{11\text{b}}$
$\text{Fe}(\text{OH})^+ + \text{H}_2\text{O} \rightleftharpoons \text{Fe}(\text{OH})_{2(\text{aq})} + \text{H}^+$	$2.51^{\text{b}}$	$1.0 \times 10^{8\text{b}}$
$\text{Zn}^{2+} + \text{H}_2\text{O} \rightleftharpoons \text{Zn}(\text{OH})^+ + \text{H}^+$	$3.16 \times 10^{5\text{b}}$	$1.0 \times 10^{10\text{b}}$
$\text{Zn}(\text{OH})^+ + \text{H}_2\text{O} \rightleftharpoons \text{Zn}(\text{OH})_{2(\text{aq})} + \text{H}^+$	$1.26 \times 10^{4\text{b}}$	$4.4 \times 10^{10\text{b}}$
$\text{Al}(\text{OH})_{3(\text{aq})} \rightleftharpoons \text{Al}(\text{OH})_{3(\text{s})}$	$3.31 \times 10^{-2\text{a}}$	$1.0 \times 10^{-6\text{a}}$
$\text{Al}(\text{OH})^{2+} + \text{Cl}^- + \text{OH}^- \rightleftharpoons \text{Al}(\text{OH})_2\text{Cl}_{(\text{s})}$	$1.32 \times 10^{3\text{c}}$	$1.0^{\text{a}}$
$2\text{Al}(\text{OH})_4^- + 4\text{Mg}^{2+} + 4\text{OH}^- + \text{CO}_3^{2-} \rightleftharpoons \text{Mg}_4\text{Al}_2(\text{OH})_{12}\text{CO}_3$	$1.0 \times 10^{5\text{d}}$	$1.0 \times 10^{-5\text{a}}$
$\text{Fe}(\text{OH})_{2(\text{aq})} \rightleftharpoons \text{Fe}(\text{OH})_{2(\text{s})}$	$1.0 \times 10^{-2\text{a}}$	$1.0 \times 10^{-6\text{a}}$
$\text{Fe}(\text{OH})_{2(\text{s})} + \frac{1}{4}\text{O}_2 \rightleftharpoons \text{FeOOH}_{(\text{s})} + \frac{1}{2}\text{H}_2\text{O}$	$1.21 \times 10^{3\text{b}}$	$1.0 \times 10^{-3\text{b}}$
$\text{Zn}(\text{OH})_{2(\text{aq})} \rightleftharpoons \text{Zn}(\text{OH})_{2(\text{s})}$	$1.0 \times 10^{-2\text{a}}$	$1.0 \times 10^{-5\text{a}}$
$\text{Zn}(\text{OH})_{2(\text{s})} + 4\text{Zn}^{2+} + 6\text{OH}^- + 2\text{Cl}^- \rightleftharpoons \text{Zn}_5(\text{OH})_8\text{Cl}_{2(\text{s})}$	$1.0 \times 10^{6\text{e}}$	$1.0 \times 10^{-22\text{a}}$
$5\text{Zn}^{2+} + 6\text{OH}^- + 2\text{CO}_3^{2-} \rightleftharpoons \text{Zn}_5(\text{OH})_6(\text{CO}_3)_2_{(\text{s})}$	$1.0 \times 10^{8\text{e}}$	$1.0 \times 10^{-30\text{a}}$

<sup>a</sup>s<sup>-1</sup>.<sup>b</sup>m<sup>3</sup> mol<sup>-1</sup> s<sup>-1</sup>.<sup>c</sup>m<sup>6</sup> mol<sup>-2</sup> s<sup>-1</sup>.<sup>d</sup>m<sup>30</sup> mol<sup>-10</sup> s<sup>-1</sup>.<sup>e</sup>m<sup>36</sup> mol<sup>-12</sup> s<sup>-1</sup>.**FIGURE 5** Steady-state current density distribution over a cut-edge surface for different metallic coatings. Position of the coating is highlighted. [Color figure can be viewed at wileyonlinelibrary.com]

more positive than the measured ones. We believe that this difference is due to the fact that it is assumed in the simulations that the coatings on both sides of the cut edge are equally active while in the reality the activity is not distributed uniformly along the coating surface, but is concentrated in few very active spots. Indeed, after introducing a “spot” with higher activity on one of the coatings, simulated cut-edge potentials become more negative.

Based on the values of the cut-edge potentials, one can expect that the protective action of AlZn0 should be very poor, while AlZn10 and especially AlZn30Mg4 coatings will protect the cut-edge. Indeed, the outcome of the simulations shows that the amount of Fe-containing solid corrosion products in case of AlZn0 coating is about five orders of magnitude higher than with the other two coatings (see Figure 6). These results are fully confirmed by the visual appearance of the samples, shown in the inset in Figure 6. It can be seen that the precipitates are distributed almost uniformly along the steel surface. The area about 100 around the metallic coating is better protected which is

**TABLE 5** Comparison of measured and simulated values of corrosion potential and minimum and maximum pH

Metallic coating	$E_{\text{corr}}$ , V		pH <sub>min</sub>		pH <sub>max</sub>	
	Simulated <sup>a</sup>	Measured	Simulated	Measured	Simulated	Measured
AlZn0	-0.635/-0.654	-0.70	4.69	4.5-4.9	10.04	9.5-9.9
AlZn10	-0.796/-0.918	-0.89	4.95	4.8-5.5	10.60	9.0-9.7
AlZn30Mg4	-0.844/-0.963	N/A	4.36	4.6-5.2	10.83	9.8-10.3

<sup>a</sup>Symmetrical activity of the metallic coatings/"active spot" × 50 on the right-side coating.

indicated by the diminished amount of Fe-containing corrosion products.

Distributions of corrosion products based on the metallic coatings components has been simulated as well. The results for different aluminum- and zinc-containing corrosion products are shown in Figure 7. Curiously, despite the fact that AlZn0 is almost pure aluminum coating, amounts of

Al(OH)<sub>2</sub>Cl<sub>(s)</sub> and Al(OH)<sub>3(s)</sub> precipitated on the cut-edge surface are minimal. This can be related to the lower activity of the AlZn0 coating in comparison to other two studied alloys.

The concentration profiles, simulated for all solid corrosion products, are converted into a layer thickness and compared with the experimental map based on the consecutive pH, SEM-EDS, and micro-Raman measurements performed over the same sites on one specific sample, see Figure 8. In order to facilitate the comparison, the layer thickness is rotated. As the simulations are two-dimensional, only a perpendicular cross-section can be considered. Nevertheless the simulated distributions show a trend very similar to the experimental observations: Al-containing corrosion products are located in the vicinity of the metallic coating, while Zn- and Mg- corrosion products are spread more toward to the middle of the steel. Analysis of Figure 8b shows that despite the fact that Zn is not the main component of the metallic coating, the layer of corrosion products consists mostly of hydrozincite Zn<sub>5</sub>(OH)<sub>6</sub>(CO<sub>3</sub>)<sub>2</sub>.

Looking into details of the distribution of solid corrosion products (see Figure 9) one can notice that when the "active spot" is introduced on one side of the cut-edge the fronts of the precipitates are not symmetrical: they are located further toward middle of the steel on the side of the more active coating. This fully corresponds to the experimentally observed behavior (see the inset of Figure 9).

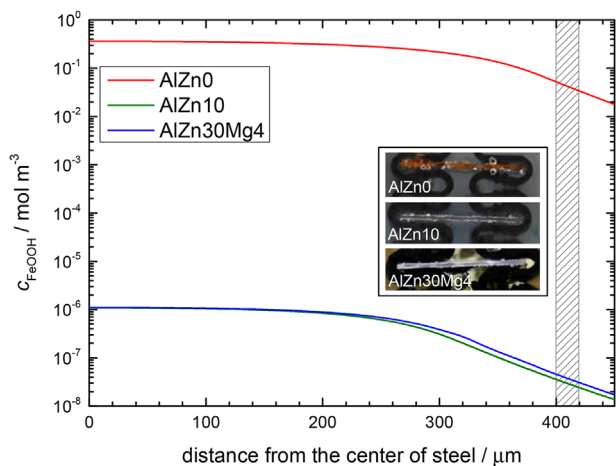


**FIGURE 6** Simulated distribution of Fe-OOH precipitates on the cut-edge surface. Position of the coating is highlighted. Inset: appearance of the samples after 50 h of immersion in 1 wt% NaCl. [Color figure can be viewed at wileyonlinelibrary.com]

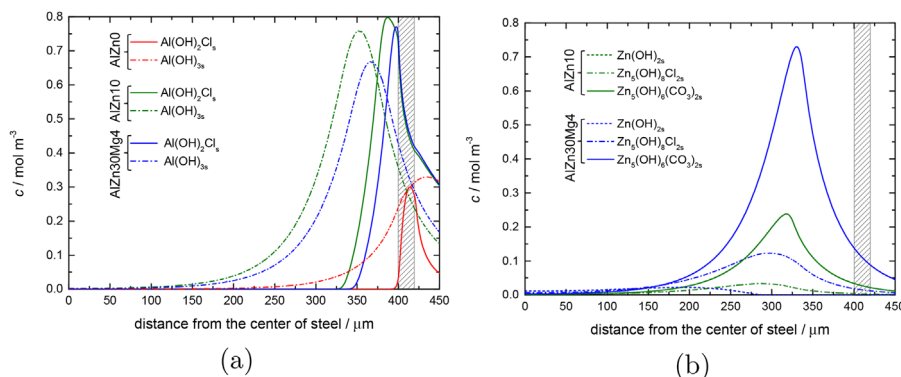


**FIGURE 7** Simulated distributions of aluminum- (a) and zinc- (b) containing solid corrosion products on the cut-edge surface. Position of the coating is highlighted. [Color figure can be viewed at wileyonlinelibrary.com]

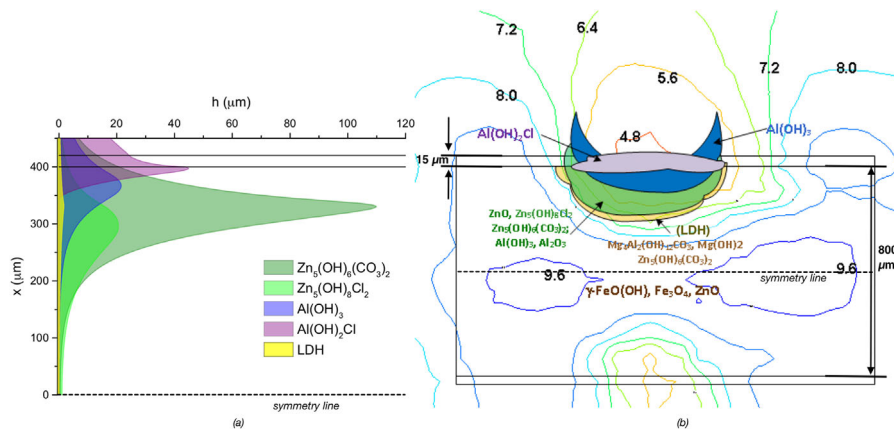


**FIGURE 8** Distribution of corrosion products above the cut-edge with AlZnMg coating: (a) simulated; (b) constructed from measurements, the values in the contour lines indicate local pH. (b) reproduced from ref. [9]. [Color figure can be viewed at wileyonlinelibrary.com]

The local pH can be estimated based on the simulated concentration of  $H^+$  ions. For the AlZn0 system (Figure 10a), a quite low pH is observed in the whole electrolyte, which is attributed to the high acidification of  $Al^{3+}$  ions. For this

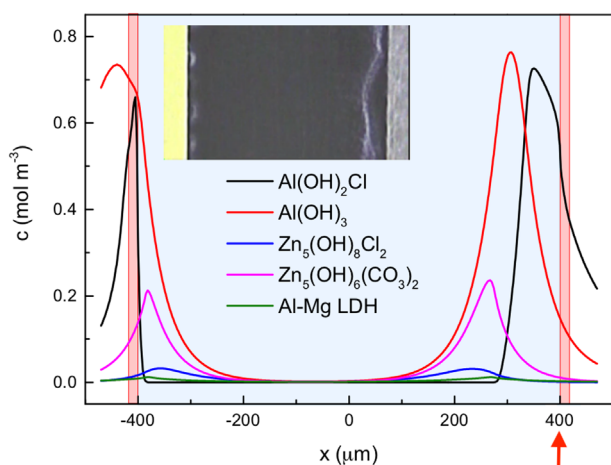


**FIGURE 9** Simulation of solid corrosion product distribution for the AlZn30Mg4 coating. Positions of the coating (red area) and active spot (red arrow) are highlighted. Inset: appearance of the sample after 20 min of immersion in 1 wt% NaCl. [Color figure can be viewed at wileyonlinelibrary.com]

coating, introducing an active spot does not directly influence the pH distribution. This is different for the AlZn30Mg4 system, shown in Figure 10(b), where the introduction of the active spot leads to a non-symmetrical distribution of pH. This is in correspondence with the distribution of the corrosion products (see Figure 9). The area of high (8.5–10.5) pH is located above steel, and the areas of low (4.2–5.5) pH are found above the metallic coatings. The pH above the more active side of the cut-edge is about 1 unit lower.

The difference between a pure aluminum coating and the zinc-containing coating has been demonstrated experimentally as well. pH maps above the sample are shown in Figure 11. The pH is measured with SIET (Scanning ion-selective electrode technique). Note that the SIET probe starts from 40  $\mu m$  above the surface and that in the simulation pH can be obtained at the sample surface.

In the case of the AlZn0-coating, higher pH values are measured than predicted with the simulations. Also in the low pH range, lower pH values are simulated than experimentally observed. The location of low and high pH correspond at the right side. At the left side however, above the coating no drop in pH is observed experimentally, possibly this is because the coating is inactive at that point.

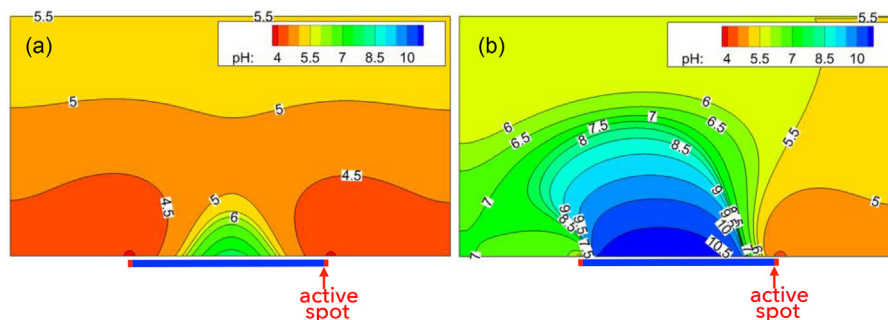


**FIGURE 10** Simulated pH distributions in the electrolyte above the cut-edge for (a) the AlZn0 coating and (b) the AlZn30Mg4 coating. [Color figure can be viewed at wileyonlinelibrary.com]

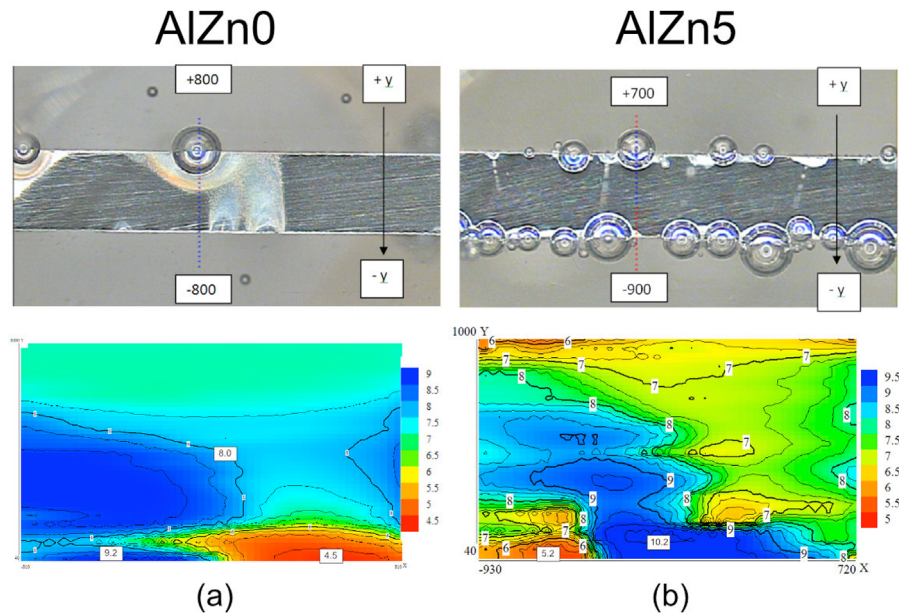


**FIGURE 11** Optical image and pH map obtained with SIET after 1 h of immersion in 1 wt% NaCl for (a) a pure aluminum coating and for (b) an aluminum coating containing 5 wt% zinc. [Color figure can be viewed at [wileyonlinelibrary.com](http://wileyonlinelibrary.com)]

The pH maps obtained with SIET give a very good qualitative validation with the simulations. However, since in the simulations no stochastic behavior is taken into account, it is very difficult to make a quantitative comparison. Furthermore, the pH maps are taken after 1 h of immersion, whereas the simulations presume steady-state conditions. Several SIET maps have been obtained during the first hours of immersion and significant changes are observed. The general conclusions are that the average pH above anodic sites containing no zinc (pure aluminum coating) are lower than above the samples with high amounts of zinc.

The AlZnMg coatings dissolve selectively, which has been shown by the AESEC measurement. Initially a parametric study is performed to reveal the effect of individual alloy components on the pH distribution and the

number of corrosion products. When only  $Zn^{2+}$  and  $Mg^{2+}$  ions are being released into the solution (initial stage of the dissolution of the AlZnMg coating), the pH is about 9.0 above the cathodic area and 6.2–8.5 above the anodic areas are simulated depending on the coating activity (see Figure 12a). When AlZn matrix starts dissolving, the minimum pH decreases about 2 units while maximum pH increases close to 1.5 units. The effect of higher acidification by  $Al^{3+}$  ions in comparison to  $Zn^{2+}$  has been found in ref. [19] when studying corrosion behavior of steel cut-edges with pure Al, pure Zn and AlZn coatings, and is related to the higher stability of aluminum hydroxyl complexes  $[Al(OH)_n]^{3-n}$  with respect to  $[Zn(OH)_n]^{2-n}$ .

Simulations also show that the amount of Zn-containing corrosion products, especially of hydrozincite  $Zn_5(OH)_6(CO_3)_2$ ,

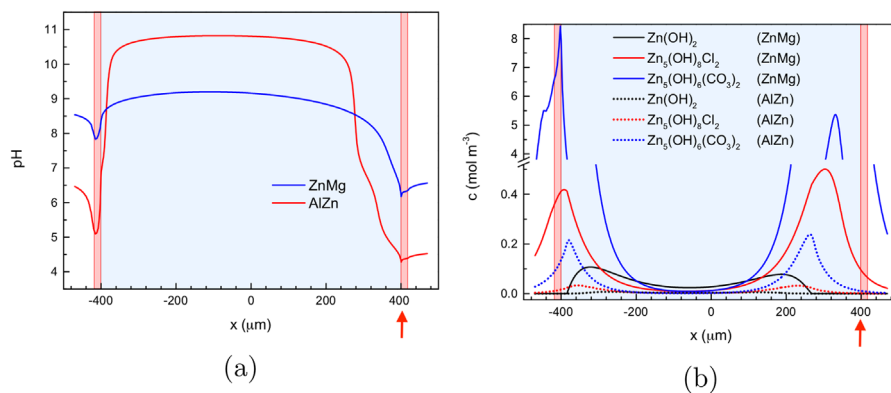


**FIGURE 12** Simulated distributions of (a) pH and (b) Zn-containing corrosion products over steel/AlZnMg cut-edge for the cases when different phases are dissolving (ZnMg and AlZn phases). Positions of the coating (red area) and active spot (red arrow) are highlighted. [Color figure can be viewed at [wileyonlinelibrary.com](http://wileyonlinelibrary.com)]

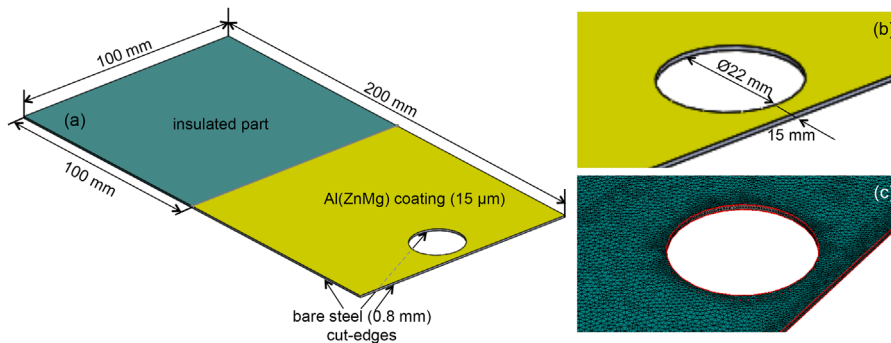


**FIGURE 13** Computational geometry and mesh used for the simulations on macro-scale. [Color figure can be viewed at wileyonlinelibrary.com]

decreases dramatically when the magnesium-containing phase is fully dissolved and only AlZn matrix is dissolving (see Figure 12b). This effect is related to the local changes of pH and might be a part of the explanation why no blocking effect has been found experimentally when studying the transport properties of corrosion products formed on steel/AlZnMg cut-edge.

#### 4 | SIMULATIONS ON A MACRO-SCALE: POTENTIAL MODEL

Although having a good prediction power, the MITReM cannot be withheld for simulations on a macro-scale level for reasons of required computational efforts and meshing size. Solving a system of equations for 30+ species on a large geometry and in time is not feasible given the current level of the computational resources. To overcome this problem, the corrosion behavior of steel cut-edges is simulated based on the potential model.

The simulations have been performed for a total period of 180 days. It is assumed that time of wetness (TOW) is one third of the total exposure time, and that a 50 µm electrolyte layer with a conductivity 0.1 S m<sup>-1</sup> is present during TOW.<sup>[20]</sup>

##### 4.1 | Governing equation and boundary conditions

Unlike MITReM, potential model does not take into account individual species in the electrolyte. It assumes that the electrolyte is perfectly mixed (no concentration gradients exist) and allows to obtain the potential distribution in the electrolyte film with constant thickness and conductivity  $\sigma$  over the substrate assembly. Governing equation of the potential model is the Laplace equation:

$$\nabla^2 U = -\frac{\delta_F}{\sigma} J_{\text{tot}} \quad (17)$$

where  $U$  (V) is the solution potential,  $\delta_F$  (m) electrolyte film thickness,  $\sigma$  (S m<sup>-1</sup>) electrolyte conductivity,  $J_{\text{tot}}$  the total

current density. The total current density is a source term along a substrate surface due to the electrochemical reactions. It is implemented as the algebraic sum of partial current densities assigned to individual electrode reactions

$$J_{\text{tot}} = \sum_i J_i \quad (18)$$

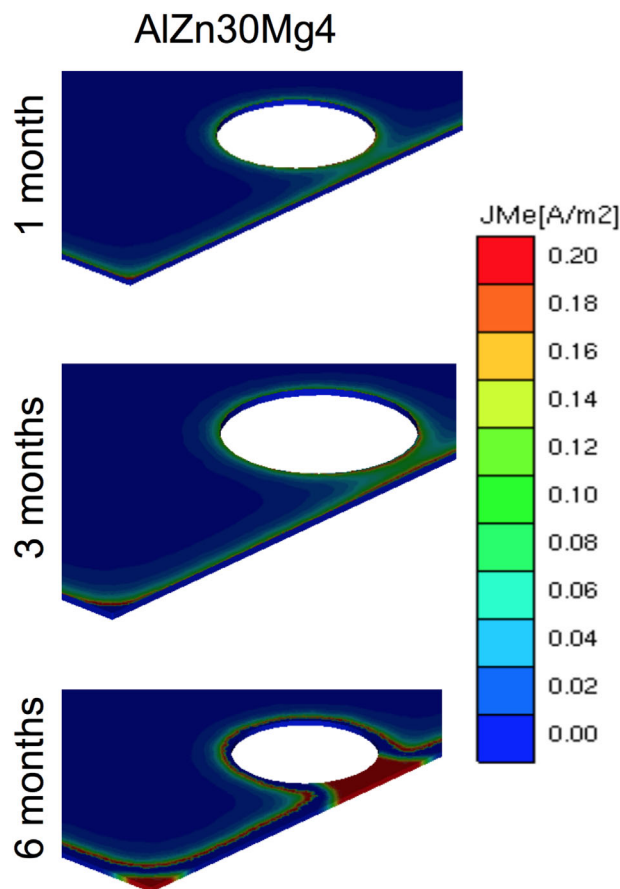


**FIGURE 14** Metal corrosion current density distribution for different stages in time. [Color figure can be viewed at wileyonlinelibrary.com]

Here essentially dissolution of the metallic coating and steel, oxygen reduction, and hydrogen evolution (Eqs. (11–14)) are considered. Kinetic parameters for these reactions are obtained with use of the Elsya CurveAnalyzer software tool that allows for pseudo-automatic decomposition of a recorded polarization curve into partial contributions.<sup>[21]</sup> In this software, partial current densities for oxygen reduction and hydrogen evolution reactions are formulated by means of the Butler–Volmer equation:

$$J_i = k_{\text{ox},i} \prod_k c_{ik} \exp\left(\frac{\alpha_{\text{ox},i} n F (V - U - E_0)}{RT}\right) - k_{\text{red},i} \prod_k c_{ik} \exp\left(-\frac{\alpha_{\text{red},i} n F (V - U - E_0)}{RT}\right) \quad (19)$$

with  $k_{\text{ox},i}$  ( $k_{\text{red},i}$ ), and  $\alpha_{\text{ox},i}$  ( $\alpha_{\text{red},i}$ ) the rate constant and charge transfer coefficient of oxidation (reduction) reaction correspondingly,  $V$  (V) electrode potential,  $E_0$  (V) standard potential. The metals oxidation reactions are fitted by spline functions.

Furthermore, the oxygen reduction reaction is diffusion controlled. Thus, the role of oxygen diffusion through the electrolyte film has to be taken into account although, strictly speaking, no concentrations can be calculated in the potential model. This is done by combining the Butler–Volmer Eq. (19) with the expression for oxygen limiting current

$$J_{\text{O}_2} = \frac{J^{\text{BV}} J^{\text{lim}}}{J^{\text{BV}} + J^{\text{lim}}} \quad (20)$$

where

$$J^{\text{lim}} = -n F D_{\text{O}_2} c_{\text{O}_2}^{\text{bulk}} \quad (21)$$

## 4.2 | Geometry and discretization

Simulations have been performed on the geometry shown in Figure 13. It represents a sample of the coated steel (0.8 mm steel, 15  $\mu\text{m}$  metallic coating) with a hole made close to one side and the upper half of the sample being insulated. The edges of the lower half are bare cut steel. For FEM calculation, this geometry is discretized in triangle elements with the refining around the hole.

## 4.3 | Results and discussion

The results of the simulations are shown in Figures 14 and 15. Figure 14 depicts the metal oxidation current, whereas Figure 15 shows the remaining sacrificial coating layer thickness, with the bare steel areas (i.e., the bare cut steel surfaces and the surfaces where the sacrificial coating has completely vanished) plotted in gray. When comparing Figure 14–15, it becomes obvious that the former clearly shows a front-line of the sacrificial coating, where the metal

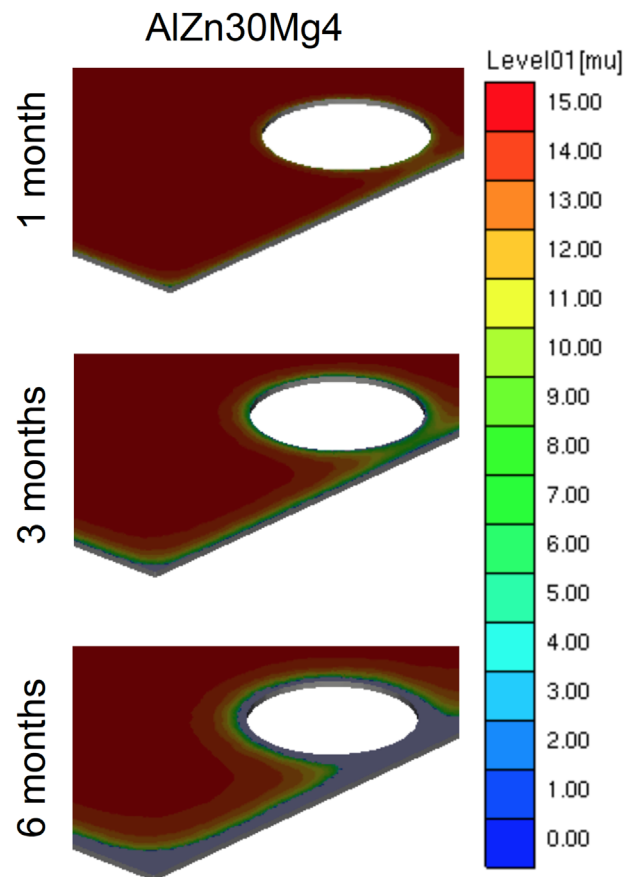


**FIGURE 15** Thickness of sacrificial Al-based coatings for different stages in time. [Color figure can be viewed at [wileyonlinelibrary.com](http://wileyonlinelibrary.com)]

oxidation of this coating is highest, followed by a bare metal zone where the corrosion current density is nearly zero. This represents an area that is sufficiently protected by the sacrificial coating. However, for later time stages (3 and 6 months), a region on the bare steel emerges where the steel starts corroding, as the regressing sacrificial coating layer is no longer capable of protecting the further away bare steel areas.

The results are compared with the observations of the outdoor test. The simulated results are in a good qualitative agreement with the observations. In order to achieve a better quantitative agreement, the model will have to be improved toward a selective dissolution of the sacrificial coating and dependence of the electrolyte film thickness on the environmental conditions.

## 5 | CONCLUSIONS

In this work, the corrosion behavior of steel–AlZnMg cut-edges immersed in a 1 wt% NaCl electrolyte solution is investigated by means of electrochemical modeling. The experimental input and validation results come from a complementary set of electrochemical and surface analytical techniques.

The multi-phase microstructure of the AlZnMg coatings leads to a non-uniform (in time) distribution of the corrosion activity. The geometrical aspect of the microstructure is not

taken into account, but the elemental composition results in a variation of the electrode kinetics. Due to different electrode kinetics of the different phases, a time-dependent dissolution takes place, which in turn determines the local and time-dependent electrolyte composition. Experiments confirm the nature and localization of the precipitated corrosion products. No experimental proof of surface protection by solid corrosion products on the steel surface with a AlZnMg coating has been found, unlike the common findings for pure zinc coatings. It is shown by simulations that the amount of hydrozincite formed in presence of  $Al^{3+}$  ions is substantially reduced. Thus, the protective action of the coating is mainly due to the initial dissolution of the magnesium-containing phase. This shifts the corrosion potential toward more electronegative potentials and provides cathodic protection.

The MITReM that describes the corrosion behavior of the studied system takes into account transport of all species in the solution, electrochemical reactions on the cut-edge surface and formation of soluble and insoluble corrosion products via various chemical reactions. The model is able to provide information about the (partial) corrosion currents and corrosion potential together with the concentration fields for all species considered in the system. The implementation of precipitation reactions for relative complex compounds allows for a validation based on corrosion product characterization. The simulations provide concentration distributions of these precipitates both in time and space. Simulated distributions of pH and precipitates are in a good agreement with measurements.

The inability to protect the steel cut-edge in the case of a pure aluminum coating has been linked to the inactivity of the coating initially. The effect of limiting cathodic protection has been studied with complementary macro-scale simulations based on the potential model. Furthermore, the corrosion products are also found only close to the cut-edge, which limits the formation of a protection layer on the steel surface. Hydrozincite is one of the corrosion products that is known to offer corrosion protection of the substrate. For the AlZnMg coating it is shown by simulations that the amount of hydrozincite formed in presence of  $Al^{3+}$  ions is substantially reduced. Thus, the protective action of the coating is mainly due to the selective dissolution of Mg-containing phase that shifts the corrosion potential toward more electronegative potentials.

## ACKNOWLEDGMENTS

This work has been carried out in the frame of the RFCS project AtCorAS “Modeling of atmospheric corrosion of steel protected by aluminium based alloys, applied by hot dip processing” (RFSR-CT-2011-00015).

## REFERENCES

- [1] S. Palani, T. Hack, J. Deconinck, H. Lohner, *Corros. Sci.* **2014**, *78*, 89.
- [2] F. Thébault, B. Vuillemin, R. Oltra, K. Ogle, C. Allély, *Electrochim. Acta* **2008**, *53*, 5226.
- [3] F. Thébault, B. Vuillemin, R. Oltra, C. Allely, K. Ogle, *Electrochim. Acta* **2012**, *82*, 349.
- [4] M. S. Venkatraman, I. S. Cole, B. Emmanuel, *Electrochim. Acta* **2011**, *56*, 8192.
- [5] S. Hœrlé, F. Mazaudier, Ph. Dillmann, G. Santarini, *Corros. Sci.* **2004**, *46*, 1431.
- [6] F. Thébault, B. Vuillemin, R. Oltra, C. Allely, K. Ogle, *Corros. Sci.* **2011**, *53*, 201.
- [7] V. Topa, A. S. Demeter, L. Hotoiu, D. Deconinck, J. Deconinck, *Electrochim. Acta* **2012**, *77*, 339.
- [8] O. Dolgikh, A. S. Demeter, A. C. Bastos, V. Topa, J. Deconinck, *Electrochem. Commun.* **2013**, *37*, 20.
- [9] O. Dolgikh, H. Simillion, S. V. Lamaka, A. C. Bastos, H. B. Xue, M. G. Taryba, A. Oliveira, C. Allély, B. Van Den Bossche, K. Van Den Bergh, J. De Strycker, J. Deconinck, *Mater. Corros.* **2018**, <https://doi.org/10.1002/maco.201810209>
- [10] C. Amatore, S. Szunerits, L. Thouin, J. S. Warkocz, *J. Electroanal. Chem.* **2001**, *500*, 62.
- [11] J. Verduin, *Limnol. Oceanogr.* **1975**, *20*, 1052.
- [12] I. Puigdomenech, *Program ‘medusa’* (make equilibrium diagrams using sophisticated algorithms). Royal Institute of Technology, Stockholm, **1992**.
- [13] J. Newman, K. E. Thomas-Alyea, *Electrochemical Systems*, 3rd ed., Wiley & Sons Inc, New York **2004**.
- [14] D. R. Lide, editor, *CRC Handbook of Chemistry and Physics*. CRC Press, Boca Raton **1999**.
- [15] O. Guseva, J. A. DeRose, P. Schmutz, *Electrochim. Acta* **2013**, *88*, 821.
- [16] W. Stumm, J. Morgan, *Aquatic Chemistry: Chemical Equilibria and Rates in Natural Waters*. John Wiley & Sons Inc, New York **1996**.
- [17] L. A. Farrow, T. E. Graedel, C. Leygraf, *Corros. Sci.* **1996**, *38*, 2181.
- [18] H. Tamura, *Corros. Sci.* **2008**, *50*, 1872.
- [19] A. Alvarez-Pampliega, S. V. Lamaka, M. G. Taryba, M. Madani, J. De Strycker, E. Tourwé, M. G. S. Ferreira, H. Terryn, *Electrochim. Acta* **2012**, *61*, 107.
- [20] N. Van den Steen, H. Simillion, O. Dolgikh, H. Terryn, J. Deconinck, *Electrochim. Acta* **2016**, *187*, 714.
- [21] *Elsyca CurveAnalyzer*. <http://www.elsyca.com/solutions/elsyca-curveanalyzer-1>

**How to cite this article:** Dolgikh O, Simillion H, Lamaka SV, et al. Corrosion protection of steel cut-edges by hot-dip galvanized Al(Zn,Mg) coatings in 1 wt% NaCl: Part II. Numerical simulations. *Materials and Corrosion*. 2018;1–13. <https://doi.org/10.1002/maco.201810210>